Improved chemical and electrochemical stability of perovskite oxides with less reducible cations at the surface

Nikolai Tsvetkov[1,2†], Qiyang Lu[1,3†], Lixin Sun[1,2], Ethan J. Crumlin[4] and Bilge Yildiz[1,2,3★]

Segregation and phase separation of aliovalent dopants on perovskite oxide (ABO_3) surfaces are detrimental to the performance of energy conversion systems such as solid oxide fuel/electrolysis cells and catalysts for thermochemical H_2O and CO_2 splitting. One key reason behind the instability of perovskite oxide surfaces is the electrostatic attraction of the negatively charged A-site dopants (for example, Sr'_{La}) by the positively charged oxygen vacancies ($V_O^{\bullet\bullet}$) enriched at the surface. Here we show that reducing the surface $V_O^{\bullet\bullet}$ concentration improves the oxygen surface exchange kinetics and stability significantly, albeit contrary to the well-established understanding that surface oxygen vacancies facilitate reactions with O_2 molecules. We take $La_{0.8}Sr_{0.2}CoO_3$ (LSC) as a model perovskite oxide, and modify its surface with additive cations that are more and less reducible than Co on the B-site of LSC. By using ambient-pressure X-ray absorption and photoelectron spectroscopy, we proved that the dominant role of the less reducible cations is to suppress the enrichment and phase separation of Sr while reducing the concentration of $V_O^{\bullet\bullet}$ and making the LSC more oxidized at its surface. Consequently, we found that these less reducible cations significantly improve stability, with up to 30 times faster oxygen exchange kinetics after 54 h in air at 530 °C achieved by Hf addition onto LSC. Finally, the results revealed a 'volcano' relation between the oxygen exchange kinetics and the oxygen vacancy formation enthalpy of the binary oxides of the additive cations. This volcano relation highlights the existence of an optimum surface oxygen vacancy concentration that balances the gain in oxygen exchange kinetics and the chemical stability loss.

Chemical instability of the perovskite oxide surfaces due to cation segregation and phase precipitation limits the performance and durability in multiple applications, including solid oxide fuel and electrolysis cells (SOFC/SOEC)[1,2], thermochemical[3] and photo-assisted[4] water splitting. State-of-the-art SOFC cathode materials, exemplified by $La_{0.6}Sr_{0.4}CoO_3$ (ref. 5), $La_{0.6}Sr_{0.4}Co_{0.2}Fe_{0.8}O_3$ (LSCF, ref. 6) and $Ba_{0.5}Sr_{0.5}Co_{0.8}Fe_{0.2}O_3$ (BSCF, ref. 7) suffer from degradation of surface chemistry and oxygen reduction reaction (ORR) kinetics at elevated temperatures[8–13]. This degradation is because of Sr segregation and separation of SrO-like insulating phases at the perovskite surface[8,11,14–17], sometimes in the form of complete coverage of the surface by SrO[15], blocking the electron transfer and oxygen exchange pathways[18] and leaving a dopant-poor subsurface region. The consequence is detrimental for electrochemical performance, by up to two orders of magnitude loss in ORR kinetics[9,10]. One method proposed to overcome this challenge has been coating of LSC[19,20] or LSCF[13] surfaces with layers of $La_{0.8}Sr_{0.2}MnO_3$[13,20] or ZrO_2[19] several nanometres in thickness. Although some enhancement in electrode stability was shown by these surface coatings, the underlying mechanisms behind the improvement of the cathode stability have not yet been revealed, making it difficult to go beyond these empirical observations.

In our previous work, the electrostatic attraction of negatively charged dopants towards a surface that is enriched with positively charged oxygen vacancies was recognized as an important driving force for Sr segregation on perovskite oxides[11]. Consequently, it is reasonable to expect that a lower concentration of oxygen vacancies could improve the surface stability and ORR kinetics. This may appear contradictory to the well-established understanding that oxygen vacancies facilitate ORR[21] and other reactions of small molecules on transition metal oxides[22–24]. However, significant degradation of the ORR kinetics because of dopant segregation and phase separation is also associated with surface oxygen vacancies[11]. Therefore, here we propose decreasing the surface oxygen vacancy concentration as a means to suppress the electrostatic driver of this detrimental process.

In this paper we hypothesized that the perovskite oxide surface stability can be tuned as a function of the reducibility of the surface. We took $La_{0.8}Sr_{0.2}CoO_3$ as a model system, and systematically modified its surface with additive cations, whose binary oxides have either lower (V^{5+})[25] or higher (Nb^{5+}, Ti^{4+}, Zr^{4+}, Hf^{4+} and Al^{3+})[25–29] enthalpies of oxygen vacancy formation compared to that of LSC[30]. We introduced these additives to the LSC surface at sub-monolayer coverages by a simple method using metal chloride solutions[31,32]. We refer to these surface-modified samples as LSC-Me, where Me denotes the added cations (see Supplementary Table 1 for details). We found that the less reducible cations, that is, Hf^{4+}, Ti^{4+}, Zr^{4+}, Nb^{5+} or Al^{3+}, improve the oxygen exchange kinetics and stability on LSC, whereas the addition of V or excess Co leads to stronger degradation. Ambient-pressure X-ray photoelectron spectroscopy

[1]Laboratory for Electrochemical Interfaces, Massachusetts Institute of Technology, 77 Massachusetts Avenue, Cambridge, Massachusetts 02139, USA. [2]Department of Nuclear Science and Engineering, Massachusetts Institute of Technology, 77 Massachusetts Avenue, Cambridge, Massachusetts 02139, USA. [3]Department of Material Science and Engineering, Massachusetts Institute of Technology, 77 Massachusetts Avenue, Cambridge, Massachusetts 02139, USA. [4]Advanced Light Source, Lawrence Berkeley National Laboratory, Berkeley, California 94720, USA. †These authors contributed equally to this work. *e-mail: byildiz@mit.edu
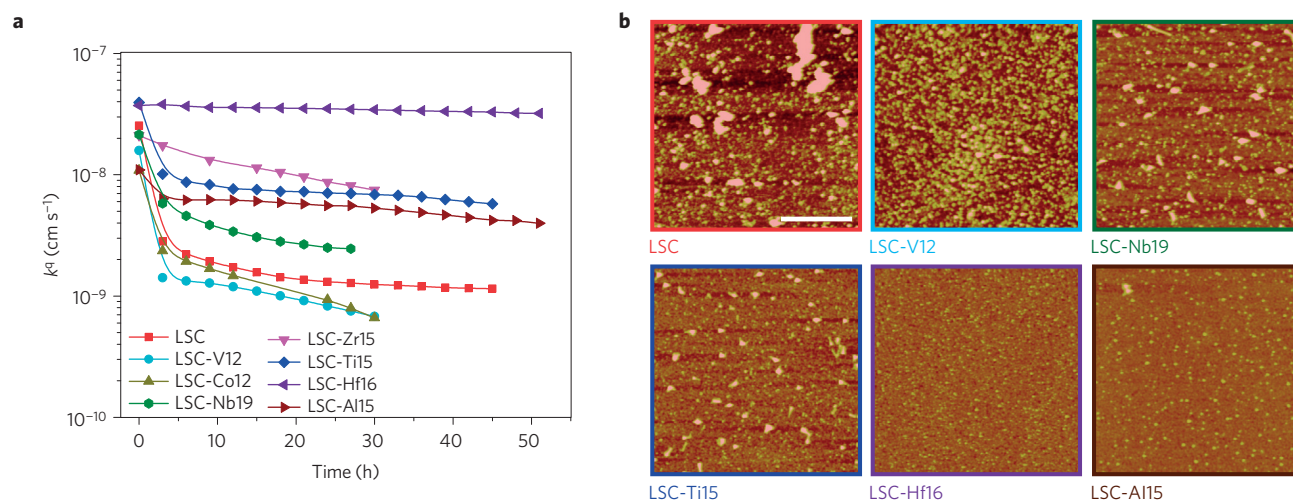
Figure 1 | Surface oxygen exchange kinetics and stability on LSC dense thin film cathodes. a, Oxygen surface exchange coefficient, k^q, quantified from electrochemical impedance spectroscopy measurements over time at 530 °C in air, for the LSC and LSC-Me films. **b**, Atomic force microscopy images of the LSC, LSC-V12, LSC-Nb19, LSC-Ti15, LSC-Hf16 and LSC-Al15 films for which the test results are shown in **a**. Scale bar, 1 μm.

(AP-XPS)[33–35] and X-ray absorption spectroscopy (AP-XAS)[36] measurements at temperatures up to 550 °C revealed that these less reducible cations increase the oxidation state of Co on the LSC surface and decrease the surface oxygen vacancy concentration, leading to a smaller electrostatic driving force for Sr segregation.

Electrochemical performance of surface-modified LSC

We compared the evolution of the surface oxygen exchange coefficients, k^q, which represents the oxygen reduction reactivity of LSC cathodes as a function of time at 530 °C in air. The LSC films treated with chloride solutions of Co, V, Nb, Zr, Ti, Hf and Al are denoted as LSC-Co12, LSC-V12, LSC-Nb19, LSC-Zr15, LSC-Ti15, LSC-Hf16 and LSC-Al15, respectively. The numbers indicate the Me/(La+Sr+Co+Me) ratio at/near the film surface. The k^q values obtained from electrochemical impedance spectroscopy (EIS) are given in Fig. 1a. Initially, all the samples have similar k^q values. Within the first few hours of the measurements, the surface exchange kinetics degraded to varying extents on the different samples. The LSC, LSC-Co12 and LSC-V12 electrodes degraded most severely, with almost 1.5 orders of magnitude decrease of k^q within the first 30 h of testing. The LSC-Ti15, LSC-Zr15, LSC-Hf16, LSC-Nb19 and LSC-Al15 cathodes were more stable, with the best performance by LSC-Hf16 having more than 30 times faster oxygen exchange kinetics than that on LSC after 54 h.

The morphology of the electrochemically tested cathode surfaces, shown in Fig. 1b, indicates the correlation of the electrochemical stability to the surface chemical stability. On the films with fast degradation of k^q, that is, LSC and LSC-V12, a high surface roughness and particle coverage is evident. Electrochemically stable films such as LSC-Ti15, LSC-Al15 and LSC-Hf16 have a more stable surface morphology with significantly lower roughness. Our previous investigation into the nature of these segregated particles on cobaltites identified them as an insulating SrO-related phase which degrades the surface oxygen exchange[8,14]. From these results, it is clear that the addition of the less reducible cations prevents the segregation of insulating Sr-rich phases, and improves the electrochemical stability and kinetics significantly (>10×) relative to pristine LSC.

Evolution of surface chemical composition

AP-XPS on the pristine LSC and the LSC-Ti3, LSC-Ti15 and LSC-Hf16 films provided more detailed assessment of the surface chemical stability. The experiments were conducted in oxygen pressures (pO_2) from 10^{-6} torr to 0.76 torr and at temperatures up to 550 °C. The analysis of the Sr 3*d* photoelectron spectra allows quantification of the atomic concentration of Sr at the film surface, and also the Sr binding environments in the perovskite lattice and in a non-lattice phase at the surface ($[Sr]_{Lattice}$ and $[Sr]_{Non-lattice}$, respectively) (Supplementary Fig. 5)[8,37]. Our chemical composition analysis showed that the total Sr content and the non-lattice Sr concentration are higher on LSC than on LSC-Ti3, LSC-Ti15 and LSC-Hf16. In particular, LSC-Ti15 and LSC-Hf16 have a significantly more stable surface Sr composition than LSC. The concentration ratio $[Sr]_{Total}/([Sr]+[La])$ at the film surfaces is shown in Fig. 2a. The LSC-Hf16 and LSC-Ti15 films showed only a small increase in the Sr content up to 550 °C. Under the same conditions, $[Sr]_{Total}/([Sr]+[La])$ increased significantly on the bare LSC and on LSC-Ti3. In the Supplementary Information, we demonstrate that the environmental temperature and oxygen pressure govern the Sr-chemistry evolution shown in Fig. 2, and not temporal variations at each condition (Supplementary Fig. 6).

The high $[Sr]_{Non-lattice}$ values on the LSC and LSC-Ti3 films (Fig. 2b) are in good agreement with the large coverage of their surface with the segregated particles detected from *ex situ* atomic force microscopy (AFM) (Fig. 2d). Thus, the $[Sr]_{Non-lattice}$ signal can be reasonably attributed to the signal from SrO-rich phase-separated areas of the films[8,14]. The LSC-Hf16 and LSC-Ti15 samples have a significantly smaller amount of $[Sr]_{Non-lattice}$ (Fig. 2b) and a much more stable surface chemistry, with relatively very small amounts of phase-separated particles at the surface (Fig. 2d).

Oxidation state on LSC-Me surfaces relative to LSC

To reveal the mechanism for improved LSC surface stability with the less reducible cations, we measured the X-ray absorption spectra near the Co $L_{2,3}$-edge and O K-edge and the valence band structure, under oxygen pressures pO_2 from 10^{-6} torr to 0.76 torr of pO_2 and at temperatures up to 550 °C. The Co $L_{2,3}$-edge spectra recorded at different conditions for the LSC-Hf16 film are given in Fig. 3a as an example. Chemical shifts of the Co L_3-edge main peak were used to estimate the change in the Co oxidation state. Figure 3b summarizes the Co L_3-edge position for LSC, LSC-Ti3, LSC-Ti15 and LSCF-Hf16 measured at 300 °C, 0.76 torr. The *x*-axis in Fig. 3b, from left to right, runs in the direction of an expected lowering of the oxygen vacancy formation enthalpy, or equivalently an expected increase of the oxygen vacancy concentration (based on the effects of Hf and Ti in different amounts). The variations of the Co L_3-edge
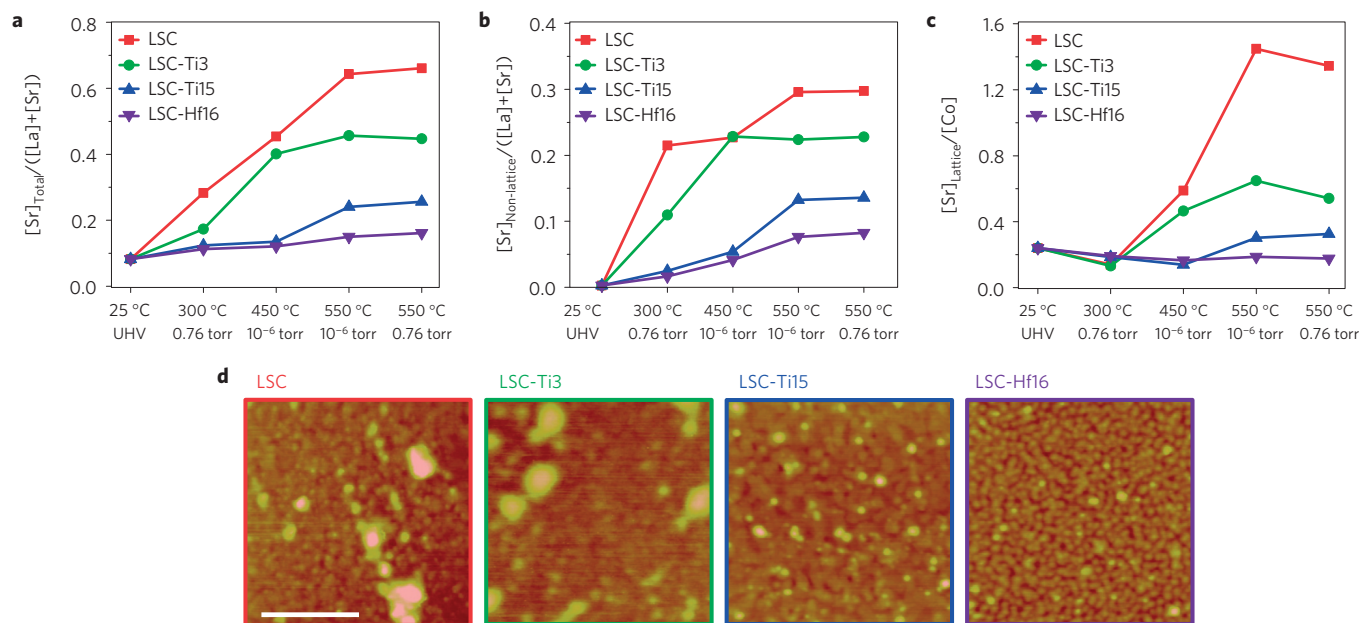
Figure 2 | Surface chemical stability on LSC dense thin films. a–c, Concentration ratios [Sr]$_{Total}$/([La]+[Sr]) (**a**), [Sr]$_{Non-lattice}$/([La]+[Sr]) (**b**) and [Sr]$_{Lattice}$/[Co] (**c**) at the surface of the LSC and LSC-Me thin films measured *in situ* at different temperatures and oxygen partial pressures by ambient-pressure X-ray photoelectron spectroscopy (AP-XPS). **d,** *Ex situ* atomic force microscopy images of the LSC and LSC-Me films following the AP-XPS measurements in **a**. Scale bar, 400 nm.
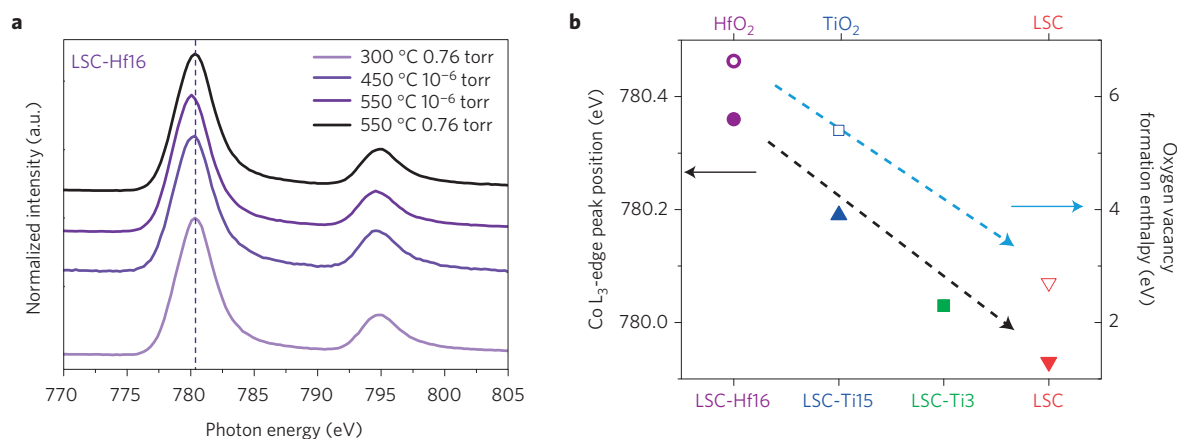
Figure 3 | Oxidation state of Co based on Co L$_{2,3}$-edge XAS on LSC dense thin films. a, Co L$_{2,3}$-edge X-ray absorption spectra on LSC-Hf16 at different temperatures and oxygen partial pressures. The dashed line marks the Co L$_3$-edge main peak at 300 °C and 0.76 torr as a reference, to monitor the relative changes in Co oxidation state. **b,** Co L$_3$-edge peak positions at 300 °C, 0.76 torr for LSC, LSC-Ti3, LSC-Ti15 and LSC-Hf16 are shown by the solid symbols. From left to right the *x*-axis shows the direction of decreasing Co oxidation state, that is, increasing oxygen vacancy concentration. The open symbols represent the oxygen vacancy formation enthalpy for the binary oxides HfO$_2$ (ref. 29) and TiO$_2$ (ref. 26), and also for LSC (ref. 30). The dashed arrows in **b** are guides to the eye and do not imply a quantitative linearity.

positions on these four samples at different conditions are provided in Supplementary Fig. 7. An increase by +1 in the Co valence, for instance, from Co^{3+} to Co^{4+}, shifts the L$_3$-edge position by about 1 eV towards higher photon energies[38]. Comparing the peak positions of Co L$_3$-edge in Fig. 3b, a clear difference in Co valence state among these samples can be seen. At 300 °C, 0.76 torr, the Co oxidation state increases on moving from LSC to LSC-Ti3, LSC-Ti15 and LSC-Hf16 (Fig. 3b). The shift in L$_3$-edge position by about +0.4 eV should correspond to an increase of the Co oxidation state by about +0.4 on LSC-Hf16 compared to that on LSC[38]. This trend, at a first glance, is contradictory to the fact that Ti^{4+} and Hf^{4+} are electron donors, assuming that these cations occupy the Co^{3+} positions in the perovskite structure. Therefore, the large difference between the L$_3$-edge positions of the unmodified LSC

and the LSC-Hf16 can be rationalized only by a difference in the oxygen vacancy concentration. That is, Hf at the surface decreases the oxygen vacancy concentration, leading to an effectively higher oxidation state of Co. This resulting trend matches qualitatively what we expect on the basis of the oxygen vacancy formation enthalpies in HfO$_2$, TiO$_2$ and LSC, also shown in Fig. 3b. An increasing Co oxidation state (that is, decreasing surface oxygen vacancy concentration) matches the trend of increasing enthalpy of oxygen vacancy formation, ΔH_f^V, such that ΔH_f^V (HfO$_2$) > ΔH_f^V(TiO$_2$) > ΔH_f^V (LSC)). Note in Fig. 3b that the dashed arrows do not imply a quantitative linearity, but are only a guide to the eye to show the qualitative relation between the Co oxidation state and the reducibility of the binary oxide of the cation added to the surface.
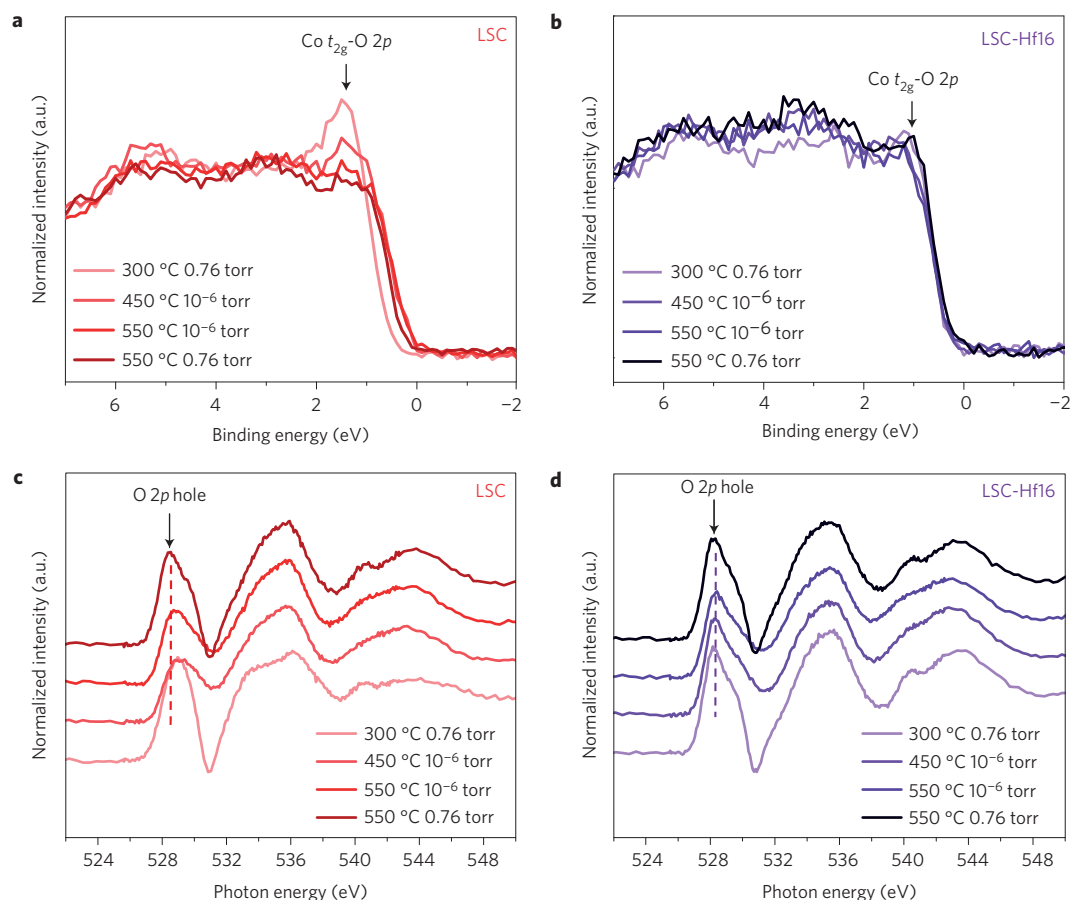
Figure 4 | Oxidation state on LSC based on the valence band and O K-edge. a,b, Evolution of the valence band structure from X-ray photoelectron spectra measured *in situ* on LSC (**a**) and LSC-Hf16 (**b**). The arrow indicates the low-energy peak, which reflects the hybridization of Co t_{2g} states with the O 2p orbital. The greater the intensity of this peak, the more electrons in the t_{2g} states of Co. **c,d**, O K-edge spectra of LSC (**c**) and LSC-Hf16 (**d**) films at different temperatures and oxygen partial pressures. The dashed lines in each plot mark the position of the O 2p ligand hole peak. The presence of this peak indicates p-type doping, and therefore an increased Co oxidation state, as seen on LSC-Ti15 and LSC-Hf16.

We have excluded the possibility that the different oxidation states from LSC to LSC-Hf16 are caused by different levels of Sr doping, as discussed based on AP-XPS results (Supplementary Section 5). It is worth noting that we have limited the comparison of the Co L_3-edge among the samples to the condition at 300 °C, 0.76 torr, before significant Sr segregation on LSC and LSC-Ti3 (Supplementary Section 5). The AP-XAS results were also supported by measuring the Co 2p core level spectrum using a laboratory X-ray source in ultrahigh vacuum at ~10^{-9} torr. We have found Co to be more difficult to reduce on the LSC modified by Nb, Ti, Zr, Hf and Al, and easier to reduce on the LSC modified by V (Supplementary Fig. 8).

We next show that the evolution of the valence band as well as the O K-edge spectra also support a more oxidized surface when LSC is modified by Hf and Ti, consistent with the Co $L_{2,3}$-edge XAS above. The valence band spectra of LSC and LSC-Hf16 films at different conditions are shown in Fig. 4a,b. For the LSC, the intense peak located close to 1.5 eV at 300 °C arises from the Co t_{2g} states hybridized with the O 2p states[39]. In contrast, on LSC-Hf16, this peak was absent at the same condition. The intensity of this peak is related to the number of electrons at the Co t_{2g} orbital[39], and provides information on the Co oxidation state. Therefore, the absence of this peak on LSC-Hf16 indicates that Co is more oxidized than on LSC, in line with the Co L-edge XAS results.

Figure 4c,d summarizes the evolution of the O K-edge spectra on LSC and LSC-Hf16 films. In line with the unchanged valence band structure (Fig. 4b), the O K-edge spectra on LSC-Hf16 remained

unaltered throughout the measurements. A sharp pre-edge peak at approximately 528 eV (shown by the arrows in Fig. 4d) indicates the existence of O 2p ligand holes on LSC-Hf16[40]. In contrast, this peak was absent on LSC at 300 °C and a pO_2 of 0.76 torr. The presence of this peak indicates an increased p-type doping level and a more oxidized Co on LSC-Hf16 compared to that on LSC.

The valence band and the O K-edge spectra for LSC film surfaces modified by different amounts of Ti are shown in Supplementary Figs 9 and 10. The evolution of the valence band and the O K-edge spectra on LSC-Ti3 were essentially similar to those of LSC. With a higher concentration of Ti, as on LSC-Ti15, the spectra were similar to those of LSC-Hf, also indicating a more oxidized Co valence at the surface.

At 450–550 °C, the valence band as well as O K-edge XAS of LSC and LSC-Hf16 become similar, with the disappearance of the Co t_{2g}–O 2p peak on LSC, as well as the appearance of the ligand hole pre-edge peak on LSC. The variations of [Sr]$_{Lattice}$ as a function of temperature can explain this behaviour. Raising the temperature to 450–550 °C substantially increases the [Sr]$_{Lattice}$/[Co] ratio (Fig. 2c) on LSC and LSC-Ti3. The higher Sr doping level in the near-surface region is charge-compensated by Co becoming more oxidized. This decreases the intensity of the Co t_{2g}-O 2p peak in the valence band and forms the O 2p ligand hole peak in the O K-edge spectra on LSC and LSC-Ti3 at 450–550 °C. As a result, at 300 °C the difference in the valence band and O K-edge among the samples is mainly due to a difference in oxygen vacancy concentrations at the surface. On the other hand, at 450–550 °C the enrichment of [Sr]$_{Lattice}$ near the
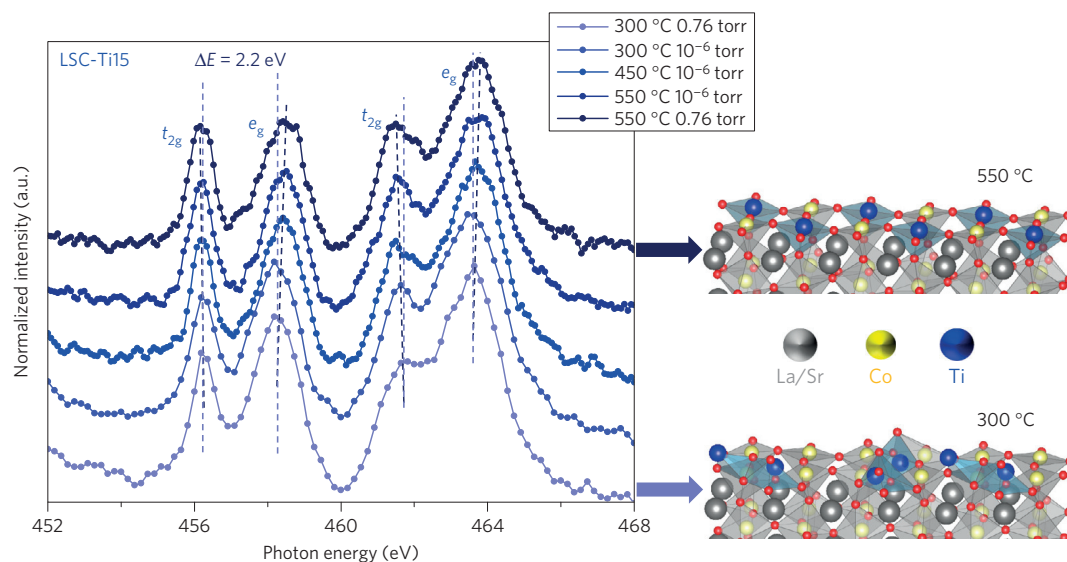
Figure 5 | Coordination environment of Ti on LSC-Ti15. Ti $L_{2,3}$-edge X-ray absorption spectra under different measurement conditions. The dashed lines mark the separation of t_{2g} and e_g peaks in both the L_2 and the L_3 edges. On the right is a schematic representation of the evolution of the Ti coordination at the LSC surface, from disordered at 300 °C to perovskite coordination of Ti atoms at the B-site of LSC at 450–550 °C (visualized using the VESTA software[47]).

surface of LSC governs the evolution of the valence band and the O K-edge spectra.

Bonding environment of the surface additive cations

AP-XAS also allows exploration of the local bonding environment of the cations added to the LSC surfaces. Fig. 5 shows the Ti $L_{2,3}$-edge on LSC-Ti15 under different measurement conditions. Each $L_{2,3}$-edge shows two peaks due to the crystal field splitting (t_{2g} and e_g states). Comparing the Ti $L_{2,3}$-edge XAS with the spectra reported in the literature for TiO$_2$[41] and SrTiO$_3$[42] (Supplementary Fig. 11), we found that the Ti cations deposited on LSC are not coordinated as in crystalline TiO$_2$. Rather, the spectral shape indicates that Ti sits in an octahedral crystal field similar to that of perovskite SrTiO$_3$[42], schematically shown in Fig. 5. This suggests that the Ti cations possibly occupy Co sites in the perovskite lattice of LSC at the surface. By occupying the B-sites in the perovskite, the presence of Ti on LSC can have a considerable effect on the electronic structure and the oxygen vacancy formation energy of LSC.

Hf, Zr or Nb could not be examined by XAS owing to the photon energy of the experiment beamline being limited to 900 eV. Nevertheless, it is known that all of the cations tested can occupy B-sites in perovskite oxides[43–46]. Therefore, we can reasonably assume that similar perovskite-like bonding environments would be obtained also for these transition metal cations (Supplementary Section 9). Their presence as dopants into the Co-site of LSC alters the oxygen vacancy formation energy at the LSC surface because the bonding between the added less reducible metal cations and oxygen is stronger than the Co–O bonds.

Balancing Sr segregation and ORR kinetics

We can now summarize the effect of the less reducible additive cations on Sr segregation. On incorporation into the perovskite lattice at the surface, the less reducible cations, $Me_{Co}^{\bullet}$, can impact the LSC electronic structure and stability in three possible ways: $Me_{Co}^{\bullet}$ decreases the surface $V_O^{\bullet\bullet}$ concentration (leading to a more oxidized Co), thus suppressing the electrostatic attraction of Sr_{La}' towards the surface; $Me_{Co}^{\bullet}$ provides donor doping and decreases the Co oxidation state; $Me_{Co}^{\bullet}$ attracts Sr_{La}' towards the surface because of its own positive charge. On the basis of the *in situ* XPS and XAS data obtained above, we found that the last two effects are not evident

and a more oxidized Co is dominant (that is, the first outcome), as shown in Figs 3, 4. This proves that the most likely main effect of the surface doping is to decrease the surface $V_O^{\bullet\bullet}$ concentration (and thus the positive charge) and relieve the electrostatic attraction of Sr_{La}' towards the surface, thereby suppressing the phase separation of Sr-rich particles (Figs 1, 2). Consequently, the less reducible cations help stabilize a surface that is more like the pristine perovskite, exposing not only the SrO-termination, but a mixed A-site and B-site (Co) presence at the surface.

It is intriguing to observe that faster and more stable oxygen exchange kinetics was achieved with a decreased oxygen vacancy concentration on LSC. This finding is shown explicitly by the volcano-like dependence of the oxygen exchange kinetic coefficient, k^q, on the difference between the enthalpy of oxygen vacancy formation in the corresponding binary oxide (that is, MeO$_x$) and that in LSC (Fig. 6). In this plot, we chose the phases of the binary oxides that are thermodynamically stable under our experimental conditions. On the basis of this plot, we propose ΔH_f^V of binary oxides MeO$_x$ as a descriptor for the stability of oxygen exchange or ORR kinetics on LSC-Me. As shown in Fig. 6, k^q increases with increasing $\Delta H_f^V(MeO_x)$, reaching a peak for LSC-Hf among the compositions tested here. A further increase of $\Delta H_f^V(MeO_x)$ leads to the slower ORR kinetics seen on LSC-Al. We attribute the increase in k^q with increasing $\Delta H_f^V(MeO_x)$ to the decreased surface oxygen vacancy concentration, which reduces the electrostatic attraction of Sr and stabilizes the surface cation composition. A further increase of oxygen vacancy formation enthalpy by adding Al onto the surface did not lead to faster ORR kinetics (although it did improve the surface composition stability, as shown in Fig. 1b), probably because of a too low concentration of surface oxygen vacancies as reactive sites. Note the similarity of this plot to the same behaviour shown as a function of varying concentration of Ti addition onto LSC (Supplementary Fig. 13). This volcano plot, to some extent, challenges the well-accepted knowledge that a high oxygen vacancy concentration is desirable in facilitating oxygen exchange kinetics on transition metal oxides[21–25]. It is true that oxygen vacancies do facilitate reactions with oxygen molecules by providing the necessary reaction sites. However, they also drive a detrimental Sr segregation process which slows down the ORR kinetics. We believe that the same concept is applicable not only to
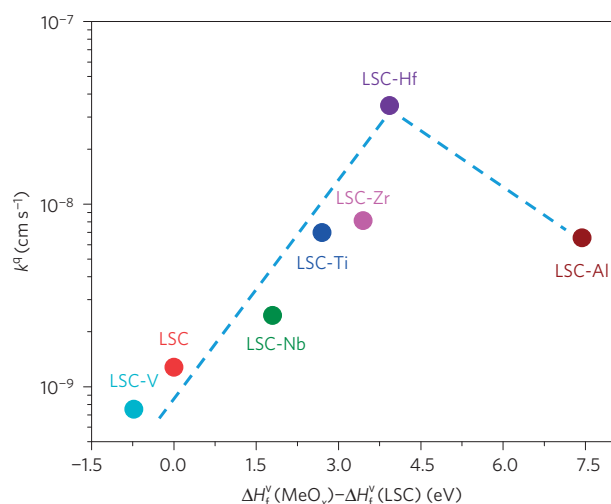
Figure 6 | Dependence of oxygen surface exchange kinetics on the reducibility of the LSC surface. The oxygen surface exchange kinetics of LSC-Me, represented by the kinetic coefficient k^q, exhibit a volcano-like dependence on the enthalpy of oxygen vacancy formation (ΔH_f^V) in the binary oxides, MeO_x. The x-axis is the difference between the ΔH_f^V of the binary oxides (that is, V_2O_5 (α-phase, orthorhombic)[25], Nb_2O_5 (α-phase, orthorhombic)[28], TiO_2 (rutile phase)[25,27], ZrO_2 (monoclinic phase)[29], HfO_2 (monoclinic phase)[29] and Al_2O_3 (α-phase, hexagonal)[26]) and that of LSC[30]. The y-axis shows k^q on LSC-Me, where the surface Me concentrations are within 12–19%, measured after 27 h of testing at 550 °C in air. The dashed line is a guide for the eye.

LSC but also to other state-of-the-art perovskite oxide catalysts, such as LSCF and BSCF.

In conclusion, we achieved significantly improved surface chemical and electrochemical stability on a model perovskite electrocatalyst, LSC, by modifying its surface with less reducible cations. The best performance was achieved by Hf modification of the surface, giving rise to 30 times faster oxygen exchange kinetics than that on the unmodified LSC after 54 h at 530 °C. There are two dominant effects on the surface chemistry of LSC due to the introduction of these cations: they reduce the Sr enrichment and phase separation into insulating particles at the surface; and they induce an effectively more oxidized surface with a lower concentration of oxygen vacancies. Both of these outcomes were consistently shown by the Co $L_{2,3}$-edge, O K-edge and the valence band structure obtained by AP-XPS/XAS. We believe that the first outcome is a consequence of the second—that is, the decrease in the surface oxygen vacancy concentration and the positive charge decreases the electrostatic driving force for Sr'_{La} segregation towards the surface and the phase separation. Ti $L_{2,3}$-edge spectra showed that the additive cations enter a perovskite-like coordination on LSC. On this basis we propose that the surface additive cations serve as dopants and can have a significant effect on the surface electronic structure and reduction enthalpy on LSC. Last, we revealed a volcano relation of the stability of the ORR kinetics to the oxygen vacancy formation energy at the surface. This volcano relation indicates that one can optimize the performance of the perovskite type electrocatalysts by finding an optimum surface oxygen vacancy concentration that balances the chemical stability loss and the gain in ORR kinetics. The proposed approach provides a feasible and novel way of designing both stable and highly reactive perovskite oxides for electrochemical and thermochemical applications.

Methods

Methods and any associated references are available in the online version of the paper.

References

1. Neagu, D., Tsekouras, G., Miller, D. N., Ménard, H. & Irvine, J. T. S. *In situ* growth of nanoparticles through control of non-stoichiometry. *Nature Chem.* **5**, 916–923 (2013).
2. Lee, K. T. & Wachsman, E. D. Role of nanostructures on SOFC performance at reduced temperatures. *MRS Bull.* **39**, 783–791 (2014).
3. Bork, A. H., Kubicek, M., Struzik, M. & Rupp, J. L. M. Perovskite $La_{0.6}Sr_{0.4}Cr_{1-x}Co_xO_{3-\delta}$ solid solutions for solar-thermochemical fuel production: strategies to lower the operation temperature. *J. Mater. Chem. A* **3**, 15546–15557 (2015).
4. Hisatomi, T., Kubota, J. & Domen, K. Recent advances in semiconductors for photocatalytic and photoelectrochemical water splitting. *Chem. Soc. Rev.* **43**, 7520–7535 (2014).
5. Hayd, J., Yokokawa, H. & Ivers-Tiffée, E. Hetero-interfaces at nanoscaled $(La,Sr)CoO_{3-\delta}$ thin-film cathodes enhancing oxygen surface-exchange properties. *J. Electrochem. Soc.* **160**, F351–F359 (2013).
6. Carter, S. *et al.* Oxygen transport in selected nonstoichiometric perovskite-structure oxides. *Solid State Ion.* **53**, 597–605 (1992).
7. Shao, Z. & Haile, S. M. A high-performance cathode for the next generation of solid-oxide fuel cells. *Nature* **431**, 170–173 (2004).
8. Cai, Z., Kubicek, M., Fleig, J. & Yildiz, B. Chemical heterogeneities on $La_{0.6}Sr_{0.4}CoO_{3-\delta}$ thin films—correlations to cathode surface activity and stability. *Chem. Mater.* **24**, 1116–1127 (2012).
9. Hjalmarsson, P., Søgaard, M. & Mogensen, M. Electrochemical performance and degradation of $(La_{0.6}Sr_{0.4})_{0.99}CoO_{3-\delta}$ as porous SOFC-cathode. *Solid State Ion.* **179**, 1422–1426 (2008).
10. Kubicek, M., Limbeck, A., Frömling, T., Hutter, H. & Fleig, J. Relationship between cation segregation and the electrochemical oxygen reduction kinetics of $La_{0.6}Sr_{0.4}CoO_{3-\delta}$ thin film electrodes. *J. Electrochem. Soc.* **158**, B727–B734 (2011).
11. Lee, W., Han, J. W., Chen, Y., Cai, Z. & Yildiz, B. Cation size mismatch and charge interactions drive dopant segregation at the surfaces of manganite perovskites. *J. Am. Chem. Soc.* **135**, 7909–7925 (2013).
12. Yi, J. & Schroeder, M. High temperature degradation of $Ba_{0.5}Sr_{0.5}Co_{0.8}Fe_{0.2}O_{3-\delta}$ membranes in atmospheres containing concentrated carbon dioxide. *J. Membr. Sci.* **378**, 163–170 (2011).
13. Zhu, X. *et al.* Development of $La_{0.6}Sr_{0.4}Co_{0.2}Fe_{0.8}O_{3-\delta}$ cathode with an improved stability via $La_{0.8}Sr_{0.2}MnO_{3-\delta}$ film impregnation. *Int. J. Hydrog. Energy* **38**, 5375–5382 (2013).
14. Chen, Y. *et al.* Segregated chemistry and structure on (001) and (100) surfaces of $(La_{1-x}Sr_x)_2CoO_4$ override the crystal anisotropy in oxygen exchange kinetics. *Chem. Mater.* **27**, 5436–5450 (2015).
15. Druce, J. *et al.* Surface termination and subsurface restructuring of perovskite-based solid oxide electrode materials. *Energy Environ. Sci.* **7**, 3593–3599 (2014).
16. Dulli, H., Dowben, P. A., Liou, S. H. & Plummer, E. W. Surface segregation and restructuring of colossal-magnetoresistant manganese perovskites $La_{0.65}Sr_{0.35}MnO_3$. *Phys. Rev. B* **62**, R14629–R14632 (2000).
17. Tellez, H., Druce, J., Kilner, J. A. & Ishihara, T. Relating surface chemistry and oxygen surface exchange in $LnBaCo_2O_{5+\delta}$ air electrodes. *Faraday Discuss.* **182**, 145–157 (2015).
18. Chen, Y. *et al.* Impact of Sr segregation on the electronic structure and oxygen reduction activity of $SrTi_{1-x}Fe_xO_3$ surfaces. *Energy Environ. Sci.* **5**, 7979–7988 (2012).
19. Gong, Y. *et al.* Stabilizing nanostructured solid oxide fuel cell cathode with atomic layer deposition. *Nano Lett.* **13**, 4340–4345 (2013).
20. Lee, D. *et al.* Enhanced oxygen surface exchange kinetics and stability on epitaxial $La_{0.8}Sr_{0.2}CoO_{3-\delta}$ thin films by $La_{0.8}Sr_{0.2}MnO_{3-\delta}$ decoration. *J. Phys. Chem. C* **118**, 14326–14334 (2014).
21. Kuklja, M. M., Kotomin, E. A., Merkle, R., Mastrikov, Y. A. & Maier, J. Combined theoretical and experimental analysis of processes determining cathode performance in solid oxide fuel cells. *Phys. Chem. Chem. Phys.* **15**, 5443–5471 (2013).
22. Bikondoa, O. *et al.* Direct visualization of defect-mediated dissociation of water on $TiO_2(110)$. *Nature Mater.* **5**, 189–192 (2006).
23. Diebold, U. The surface science of titanium dioxide. *Surf. Sci. Rep.* **48**, 53–229 (2003).
24. Schaub, R. *et al.* Oxygen vacancies as active sites for water dissociation on rutile TiO_2. *Phys. Rev. Lett.* **87**, 266104 (2001).
25. Ganduglia-Pirovano, M. V., Hofmann, A. & Sauer, J. Oxygen vacancies in transition metal and rare earth oxides: current state of understanding and remaining challenges. *Surf. Sci. Rep.* **62**, 219–270 (2007).
26. Carrasco, J., Lopez, N. & Illas, F. First principles analysis of the stability and diffusion of oxygen vacancies in metal oxides. *Phys. Rev. Lett.* **93**, 225502 (2004).

27. Janotti, A. *et al*. Hybrid functional studies of the oxygen vacancy in TiO_2. *Phys. Rev. B* **81**, 085212 (2010).

28. Kofstad, P. & Anderson, P. B. Gravimetric studies of the defect structure of α-Nb_2O_5. *J. Phys. Chem. Solids* **21**, 280–286 (1961).

29. Zheng, J. X., Ceder, G., Maxisch, T., Chim, W. K. & Choi, W. K. First-principles study of native point defects in hafnia and zirconia. *Phys. Rev. B* **75**, 104112 (2007).

30. Mizusaki, J., Mima, Y., Yamauchi, S., Fueki, K. & Tagawa, H. Nonstoichiometry of the perovskite-type oxides $La_{1-x}Sr_xCoO_{3-\delta}$. *J. Solid State Chem.* **80**, 102–111 (1989).

31. Sommeling, P. M. *et al*. Influence of a $TiCl_4$ post-treatment on nano-crystalline TiO_2 films in dye-sensitized solar cells. *J. Phys. Chem. B* **110**, 19191–19197 (2006).

32. Tsvetkov, N. A., Larina, L. L., Shevaleevskiy, O., Al-Ammar, E. A. & Ahn, B. T. Design of conduction band structure of TiO_2 electrode using Nb doping for highly efficient dye-sensitized solar cells. *Prog. Photovolt. Res. Appl.* **20**, 904–911 (2012).

33. Salmeron, M. & Schlögl, R. Ambient pressure photoelectron spectroscopy: a new tool for surface science and nanotechnology. *Surf. Sci. Rep.* **63**, 169–199 (2008).

34. Feng, Z. A., El Gabaly, F., Ye, X., Shen, Z.-X. & Chueh, W. C. Fast vacancy-mediated oxygen ion incorporation across the ceria–gas electrochemical interface. *Nature Commun.* **5**, 4374 (2014).

35. Grass, M. E. *et al*. New ambient pressure photoemission endstation at Advanced Light Source Beamline 9.3.2. *Rev. Sci. Instrum.* **81**, 053106 (2010).

36. Mueller, D. N., Machala, M. L., Bluhm, H. & Chueh, W. C. Redox activity of surface oxygen anions in oxygen-deficient perovskite oxides during electrochemical reactions. *Nature Commun.* **6**, 6097 (2015).

37. Crumlin, E. J. *et al*. Surface strontium enrichment on highly active perovskites for oxygen electrocatalysis in solid oxide fuel cells. *Energy Environ. Sci.* **5**, 6081–6088 (2012).

38. Hu, Z. *et al*. Difference in spin state and covalence between $La_{1-x}Sr_xCoO_3$ and $La_{2-x}Sr_xLi_{0.5}Co_{0.5}O_4$. *J. Alloys Compd.* **343**, 5–13 (2002).

39. Mizokawa, T. *et al*. Photoemission and X-ray-absorption study of misfit-layered (Bi,Pb)-Sr-Co-O compounds: electronic structure of a hole-doped Co-O triangular lattice. *Phys. Rev. B* **64**, 115104 (2001).

40. Moodenbaugh, A. *et al*. Hole-state density of $La_{1-x}Sr_xCoO_{3-\delta}$ ($0 \sim x \sim 0.5$) across the insulator/metal phase boundary. *Phys. Rev. B* **61**, 5666–5671 (2000).

41. Thomas, A. G. *et al*. Comparison of the electronic structure of anatase and rutile TiO_2 single-crystal surfaces using resonant photoemission and X-ray absorption spectroscopy. *Phys. Rev. B* **75**, 035105 (2007).

42. van der Laan, G. Polaronic satellites in X-ray-absorption spectra. *Phys. Rev. B* **41**, 12366–12368 (1990).

43. Abbate, M. *et al*. Electronic structure and spin-state transition of $LaCoO_3$. *Phys. Rev. B* **47**, 16124–16130 (1993).

44. Copie, O. *et al*. Structural and magnetic properties of Co-doped (La,Sr)TiO_3 epitaxial thin films probed using X-ray magnetic circular dichroism. *J. Phys. Condens. Matter.* **21**, 406001 (2009).

45. Fabricius, G. *et al*. Electronic structure of cubic $SrHfO_3$: ferroelectric stability and detailed comparison with $SrTiO_3$. *Phys. Rev. B* **55**, 164–168 (1997).

46. Lee, J. *et al*. Imprint and oxygen deficiency in (Pb,La)(Zr,Ti)O_3 thin film capacitors with La-Sr-Co-O electrodes. *Appl. Phys. Lett.* **66**, 1337–1339 (1995).

47. Momma, K. & Izumi, F. VESTA 3 for three-dimensional visualization of crystal, volumetric and morphology data. *J. Appl. Crystallogr.* **44**, 1272–1276 (2011).

Author contributions

N.T. and Q.L. prepared the samples. N.T. performed electrochemical measurements. Q.L., N.T., B.Y. and E.J.C. performed XPS and XAS measurements. All authors analysed and discussed the results and wrote the paper. B.Y. designed and supervised the research.

Additional information

Supplementary information is available in the online version of the paper. Reprints and permissions information is available online at www.nature.com/reprints. Correspondence and requests for materials should be addressed to B.Y.

Competing financial interests

The authors declare no competing financial interests.

Methods

Film fabrication and additive cation deposition at the surface. Dense $La_{0.8}Sr_{0.2}CoO_3$ films were deposited onto substrates using pulsed laser deposition (PLD) with a KrF excimer laser of 248 nm wavelength. The $La_{0.8}Sr_{0.2}CoO_3$ target was purchased from MTI Corp., USA. The films were deposited at 650 °C under oxygen pressure of 10 mtorr on the single-crystalline $Yr_{0.08}Zr_{0.92}O_2$ (YSZ) (100) substrates (MTI Corp., USA) with a 15-nm-thick $Gd_{0.2}Ce_{0.8}O_2$ interlayer grown at the same conditions as the LSC films. The LSC film thickness was around 25 nm. After the growth process, the films were cooled down to room temperature under an oxygen pressure of 2 torr.

To remove excess Sr and to modify the surface with the metal cations, the LSC thin films were dipped in aqueous chloride solutions of the corresponding metals[31,32]. The deposition parameters are summarized in Supplementary Table 1. For samples which were not treated with the metal cations, the excess surface Sr-rich phase formed during the PLD process was removed by dipping the films into a 0.1 M HCl aqueous solution for 10 s at room temperature[10]. After the chemical treatment the films were washed with water and isopropanol, then dried in an air flow at 260 °C for 1 min.

Surface chemical composition and morphology of the modified LSC films. We examined the chemical composition and morphology at the surface of the LSC films and the modified LSC films (LSC-Me) using X-ray photoelectron spectroscopy (XPS) and atomic force microscopy (AFM). The XPS core level peak shapes and atomic fractions of Co, La and Sr were similar for the as-prepared LSC and LSC-Me films. The LSC-Me films also had comparable additive cation fractions, defined as Me/(La+Sr+Co+Me), of 12–19% at the surface (see Supplementary Section 1). The films treated with chloride solutions of Co, V, Nb, Zr, Ti, Hf and Al are denoted as LSC-Co12, LSC-V12, LSC-Nb19, LSC-Zr15, LSC-Ti15, LSC-Hf16 and LSC-Al15, respectively, where the numbers indicate the Me/(La+Sr+Co+Me) ratio at/near the film surface. The surface morphology of the LSC-Me films in their as-prepared condition was smooth, identical to that of the dilute-HCl-treated LSC (Supplementary Fig. 1). Thus, we believe that the metal additive is deposited in the form of a thin and smooth wetting layer at room temperature before further annealing.

Characterization. A Veeco/Digital Instrument Nanoscope IV was used to perform tapping-mode AFM to characterize the surface morphology. *Ex situ* XPS measurements have been performed to estimate the surface cation composition using a Perkin-Elmer PHI-5500 ESCA Spectrometer with monochromatic Al Kα (1486.65 eV) X-ray source under a base pressure of 10^{-9} torr with an emission angle of 20°. In this configuration, the photoelectron inelastic mean free paths (IMPFs) for La 3d, Sr 3d, Co 2p, V 2p, Ti 2p, Nb 3d, Zr 2p and Hf 4d are 0.3 nm, 0.7 nm, 0.3 nm, 0.4 nm, 0.4 nm, 0.6 nm, 0.6 nm and 0.6 nm, respectively. Quantitative analysis of the XPS spectra was performed using the Multipack 9.0 software. XPS experiments at 450–500 °C and at pressure of 10^{-9} torr were performed to observe the reduction features in the Co 2p peak (with a photoelectron emission angle 90° and an IMFP of ∼1 nm), using an Omicron DAR 400 Mg/Al dual-anode non-monochromated X-ray source, an Omicron EA 125 hemispherical analyser and an Al Kα X-ray source.

EIS measurements were performed on asymmetrical cells with the LSC thin film working electrodes grown on YSZ single crystal substrates. Dense platinum current collectors in the form of a grid ($25 \times 25\,\mu m^2$ of open area in every $50 \times 50\,\mu m^2$ repeat unit over the total $7.3 \times 7.3\,mm^2$ current collector area) were deposited on the LSC thin films by means of photolithography and radiofrequency sputtering. A porous Ag layer served as the counter electrode. Platinum wire leads were connected to the current collector and the counter electrode by means of a lab-designed mechanical clip made of Pt–Ir 20% alloy wire (4N purity, ESPI

metals, Ashland, Oregon, US). A Parstat 2273 potentiostat was used to perform the EIS measurements in the frequency range 100 kHz–1 mHz with an a.c. amplitude of 5 mV and 0 V d.c. bias at 530 °C in air for durations of up to 54 h.

The half-cells for electrochemical tests used the LSC or LSC-Me thin films as the working electrode and the pasted porous Ag as the counter electrode. The EIS data obtained on the cells (Supplementary Fig. 4) were modelled with circuits consisting of two R∥CPE (a resistor in parallel with a constant phase element; Supplementary Fig. 4)[48]. The k^q values were calculated from the surface polarization resistance (arc in the lower frequency region[48,49]) data measured by EIS[50]. Details about the k^q calculations are given in Supplementary Section 3. For selected compositions, two to three samples were tested electrochemically (Supplementary Fig. 12). Variation of the measured k^q values ranged from ±10% for bare LSC to ±40% for LSC-Hf, in part because of the variability in the PLD-prepared base LSC films, and in part because of the different concentrations of additives that were introduced at the surface. The results for LSC, LSC-Ti15 and LSC-Hf16 shown in Fig. 2 represent a batch of samples that were deposited at the same time to ensure consistency of the base film. Regardless of the batch of samples, the general trend shown in Fig. 2 reveals the significantly better stability and higher k^q are consistent among all samples with the less reducible additives at the surface. ZView software was used for the data fitting and analysis.

***In situ* ambient-pressure X-ray photoelectron and absorption spectroscopy.** Ambient pressure XPS/XAS measurements at elevated temperatures on surfaces of LSC and LSC-Me thin films were performed at Beamline 9.3.2 of the Advanced Light Source, Lawrence Berkeley National Laboratory. The LSC thin films were placed on a ceramic heater, with thermocouples mounted directly onto the surfaces for surface temperature measurement. The XPS/XAS spectra were collected under the following conditions of temperature, T, and oxygen pressure, pO_2: $T = 300$ °C, $pO_2 = 0.76$ torr; $T = 450$ °C, $pO_2 = 1 \times 10^{-6}$ torr; $T = 550$ °C, $pO_2 = 1 \times 10^{-6}$ torr; $T = 550$ °C, $pO_2 = 0.76$ torr. At each condition, samples were equilibrated for 30 min before the measurement, with the XPS and XAS measurements at each condition taking about 2–3 h in total. The XPS spectra were collected at an incident photon energy of 370 eV, in the following order: a low-resolution survey with a binding energy of 200 eV∼−10 eV, then high-resolution scans of Sr 3d, La 4d, Co 2p and valence band. The IMFP for the photoelectrons was below 0.8 nm for all the spectra collected. For each condition, the XAS spectra of the O K-edge and Co $L_{2,3}$-edge were collected immediately after the XPS measurement. The O K-edge and Co L-edge spectra were collected in the photon energy ranges 515–580 eV and 760–810 eV, respectively. The XAS spectra were collected using the partial electron yield mode, with electron kinetic energies of 275 eV and 589 eV for the O K-edge and Co L-edge, respectively. This yields the IMFPs of emitted electrons as ∼0.7 nm for the O K-edge and ∼1.1 nm for the Co L-edge. Normalization of XAS spectra was performed using the ATHENA software[51].

References

48. Adler, S. B. Factors governing oxygen reduction in solid oxide fuel cell cathodes. *Chem. Rev.* **104,** 4791–4844 (2004).
49. Jamnik, J. & Maier, J. Generalised equivalent circuits for mass and charge transport: chemical capacitance and its implications. *Phys. Chem. Chem. Phys.* **3,** 1668–1678 (2001).
50. Baumann, F. S., Fleig, J., Habermeier, H.-U. & Maier, J. Impedance spectroscopic study on well-defined (La,Sr)(Co,Fe)O$_{3-\delta}$ model electrodes. *Solid State Ion.* **177,** 1071–1081 (2006).
51. Ravel, B. & Newville, M. ATHENA, ARTEMIS, HEPHAESTUS: data analysis for X-ray absorption spectroscopy using IFEFFIT. *J. Synchrotron Radiat.* **12,** 537–541 (2005).